

# CALPHAD-Based Modeling and Experimental Validation of Silicon Effect on the Solidification Behavior of Novel SiNb Cast Irons



GÜLŞAH AKTAŞ ÇELİK, Ş. HAKAN ATAPEK, ŞEYDA POLAT,  
and GREGORY N. HAIDEMENOPOULOS

The low oxidation resistance of SiMo ductile cast irons used as exhaust manifold material at high temperatures necessitates the development of new generation ductile cast iron compositions. New alloy designs can be made using CALPHAD methodology, and solidification sequence, segregation and critical phase transformation temperatures can be determined, especially for the solidified bulk materials. Thus, in commercial practicality, castable compositions with a raised  $A_1$  temperature can be obtained. In this study, novel SiNb cast irons with varying silicon contents were developed as candidate materials for exhaust manifolds. Solidification sequence, microsegregation, phase transformations, equilibrium phases of hypereutectic compositions containing 4 to 7 wt pct Si were calculated by CALPHAD-based modeling. The bulk materials of the studied compositions were cast as Y blocks and metallurgical analyzes were carried out. Studies revealed that; (i) in the ferritic matrix of the cast irons, graphite, Nb-rich carbides and some pearlite existed, (ii) pearlite formation was due to the negative segregation of silicon and positive segregation of manganese during solidification, (iii) as silicon content increased the amount of silicon dissolved in ferrite phase increased in the solidified structure and as a result pearlite formation decreased at the cell boundaries, and amount of vermicular graphite increased, (iv) depending on the silicon content the critical  $A_1$  temperature varied between 860 °C to 1013 °C and these values were higher than that of SiMo cast iron. All these findings revealed that SiNb cast irons had phase stability at higher temperatures compared to SiMo cast iron.

<https://doi.org/10.1007/s11661-024-07409-5>  
© The Author(s) 2024

## I. INTRODUCTION

AT present there are many vehicles having a variety of motor power and the need for high power engines are increasing day by day.<sup>[1]</sup> In the meantime, environmental concerns related to detrimental effects of exhaust emissions result in more restrict regulations.<sup>[2]</sup> Both of these conditions bring the requirements for an increase in specific power output of the engines. As the power output of the engines increases, the heat produced by the combustion of fuel increases and exhaust gas

temperatures reach as high as 1000 °C.<sup>[3]</sup> Thus, exhaust manifold materials having high temperature mechanical and chemical stability at reasonable cost are needed.<sup>[4-6]</sup>

The materials currently used for exhaust manifolds are either stainless steels or ductile cast irons having ferritic and/or austenitic matrices.<sup>[7-9]</sup> Among them the mostly used one is SiMo ferritic ductile cast iron that meets ASTM A1095-15 standard, and it can perform up to 750 °C. However, it has to be modified for use at higher temperatures in place of costly stainless steels<sup>[10,11]</sup> and Ni-resist alloys.<sup>[12]</sup> Modification is provided either by alloying elements like aluminum<sup>[13-16]</sup> chromium,<sup>[13,17,18]</sup> nickel<sup>[18]</sup> or by changing silicon<sup>[14,19]</sup> and molybdenum<sup>[20]</sup> content in order to increase the maximum service temperature by increasing  $A_1$  temperature and enhance not only mechanical properties but also oxidation resistance.<sup>[13,18,21,22]</sup> In SiMo cast irons, silicon and chromium solutes present in the bcc matrix are responsible for extending the ferritic phase field thus shifting  $A_1$  to higher values.<sup>[14]</sup> Besides these solutes, thermodynamical calculations on the alloying effect on  $A_1$  temperature have revealed that the addition of

GÜLŞAH AKTAŞ ÇELİK, Ş. HAKAN ATAPEK, and ŞEYDA POLAT are with the Laboratory of High Temperature Materials, Department of Metallurgical and Materials Engineering, Faculty of Engineering, Kocaeli University, Umuttepe Campus, 41001 Izmit, Turkey. Contact e-mail: [hatapek@gmail.com](mailto:hatapek@gmail.com) GREGORY N. HAIDEMENOPOULOS is with the Laboratory of Materials, Department of Mechanical Engineering, University of Thessaly, 38334 Vólos, Greece.

Manuscript submitted August 30, 2023; accepted April 4, 2024.

aluminum to commercial SiMo cast iron increases this critical temperature.<sup>[14,23]</sup> It is a fact that silicon, aluminum, and chromium that have solubility in ferrite make the cast iron harder by solute solution hardening mechanism while carbide forming elements like chromium and molybdenum enhance mechanical properties through precipitation hardening mechanism.<sup>[17]</sup> Although molybdenum is a main carbide forming element, it has a decreasing effect on  $A_1$  temperature<sup>[23]</sup> and also causes a decrease in fatigue resistance and toughness due to the precipitation of Mo-rich carbides at cell boundaries.<sup>[17,24]</sup> The effect of modifying elements on the oxidation behavior of SiMo cast irons has been extensively studied and the findings have shown that alloying elements like Si, Al, Cr and Ni increase the oxidation resistance by forming stable oxide layers on the surface.<sup>[13,14,18]</sup> Among all these alloying elements silicon and aluminum are the only ones that provide higher  $A_1$  temperature, higher mechanical properties, and better oxidation resistance at the same time.<sup>[25]</sup>

In order to eliminate the detrimental effects of molybdenum, a new cast iron has been designed by Aktaş Çelik *et al.* by replacing it with a carbide forming element like Nb that provides higher  $A_1$  temperature and causes homogeneously distributed carbides in the matrix, not at the cell boundaries.<sup>[21,25]</sup> In these studies, it is aimed to (i) provide a similar  $C_{eq}$  as conventional SiMo cast iron, (ii) keep silicon content at 4 wt pct to benefit from its enhancing effect on both  $A_1$  temperature and oxidation resistance and (iii) investigate the results of aluminum addition (up to 4 wt pct) on phase transition, microstructural features, and oxidation behavior in air atmosphere. Recently González-Martínez *et al.* have reported that microstructural features, phase transformation and mechanical properties of the ferritic ductile cast iron are strongly affected by the silicon addition up to 9.12 wt pct Si.<sup>[26,27]</sup> The findings show that although silicon has a detrimental effect on graphite nodularity, as the silicon content increases,  $A_1$  temperatures of the studied cast irons increase.<sup>[26]</sup> However, reasonable mechanical properties are obtained by the addition of silicon up to 5.34 wt pct.<sup>[27]</sup> These results indicate a need for studying the effect of silicon content in the newly developed SiNb cast iron and in this study thermodynamical calculations and their experimental verification are carried out on  $x$ SiNb ( $x$ : 4 to 7 wt pct) cast irons.

## II. COMPUTATIONAL METHOD

Thermodynamical calculations are carried out using Thermo-Calc software TCFE6 database. In the calculations, the compositions listed in Table I are used. The amount of carbon varies in the studied cast irons because it is aimed to provide a carbon equivalent ( $C_{eq}$ ) that will give a hypereutectic composition and enhance the primary graphitization. Thus, the carbon content decreases with respect to the increasing silicon amount according to the formula given in Eq. [1]. In the selected compositions, the  $C_{eq}$  value is provided as to be above 4.3 in order to ensure hypereutectic composition.

**Table I. Chemical Compositions Used in Thermo-Calc Calculations (Wt Pct)**

Cast Iron	C	Si	Nb	Mn	Ni
4SiNb	3.50	4.00	1.00	0.15	0.05
5SiNb	3.20	5.00			
6SiNb	3.00	6.00			
7SiNb	2.80	7.00			



Fig. 1—A macro image of Y block.

$$C_{eq} = C + \frac{1}{3}(Si + P) \quad [1]$$

In the calculations for each cast iron; (i) carbon isopleths indicating the equilibrium phases are plotted as composition versus temperature, (ii) critical temperatures like liquidus temperature ( $T_L$ ), solidus temperature ( $T_S$ ), austenite-ferrite transformation temperature ( $A_1$ ) are determined, (iii) solidification sequences are followed using the Scheil module, (iv) microsegregation is monitored during solidification, and (v) the amount of stable phases at room temperature ( $RT$ ) are found.

## III. EXPERIMENTAL PROCEDURE

### A. Production of the Cast Irons

Cast irons are produced by sand mold casting as Y blocks according to ASTM A536-84 standard (Figure 1). The charge is prepared using nodular pig iron (4.30 wt pct C, 0.7 wt pct Si), ferrosilicon (72 wt pct Si), ferriobium (70 wt pct Nb) and DIN 1020 steel. The melting process is carried out using a laboratory

**Table II. Chemical Compositions of the Cast Irons Obtained by OES (Wt Pct)**

Cast Iron	C	Si	Nb	Mg	Mn	P	S	$C_{eq}$
4SiNb	3.57	4.04	0.96	0.074	0.23	0.057	0.028	4.66
5SiNb	3.21	5.06	0.97	0.081	0.23	0.057	0.028	4.86
6SiNb	3.08	6.04	1.06	0.080	0.22	0.059	0.027	5.00
7SiNb	2.85	7.06	1.05	0.075	0.22	0.057	0.028	5.13

scale (25 kg) induction furnace (Inductotherm, 35 kW) and completed at 1560 °C. Spheroidization process is performed in a SiC crucible using a nucleation agent (75 wt pct Si, 0.94 wt pct Ca, 1.68 wt pct Ce, 0.89 wt pct Al) and a magnesium rich alloy FeSiMg (45 wt pct Si, 7 wt pct Mg). In order to verify the chemical composition, a sample is taken from the molten alloy and analyzed by optical emission spectrometer (OES, Foundry Master). Table II shows the chemical compositions of the cast irons and good agreement is achieved with the compositions used in Thermo-Calc calculations. The casting process is repeated until (i) nominal compositions are reached, (ii) nodular graphite morphology is attained, and (iii) casting defects (*i.e.* blowholes, open holes, pinholes and shrinkage cavity, *etc.*) are avoided.

### B. Characterization of the Cast Irons

In order to verify the thermodynamic calculations, cast irons are characterized by microstructural examinations and thermal analyses. Thus, phases formed during solidification, transition temperatures (especially  $A_1$ ) and stable phases within the solidified structure are obtained. The samples are taken from the marked region of Y block given in Figure 1 according to the ASTM A536-84 standard. A standard metallographic procedure is carried out and polished samples are etched by 3 pct Nital solution. In microstructural characterization, polished cast irons are examined by light microscope (LM, Olympus BX41M-LED) and etched cast irons are characterized by scanning electron microscope (SEM, Jeol JSM 6060) and energy dispersive spectrometer (EDS, IXRF). Both morphology and amount of graphite embedded in the matrix are quantified according to ISO 945-2, by image analyzer (IA, Leica Las V4.12). In order to identify the phases within the solidified structure, X-ray diffraction studies (XRD, Rigaku Ultima+) are carried out using Cu  $K_\alpha$  radiation and a scanning speed of 1.0 deg  $\text{min}^{-1}$ . Differential Thermal Analyzer (DTA, Netzsch STA 409 PG Luxx) is used by heating the samples to 1460 °C with a heating rate of 5 °C  $\text{min}^{-1}$  and then cooling to room temperature with a rate of 5 °C  $\text{min}^{-1}$  in order to verify the solidification characteristics and phase transition in cooling.

## IV. RESULTS AND DISCUSSION

### A. Phase Calculation and Microstructural Features of Cast Irons

The C-isopleths for SiNb cast irons having different silicon contents are given in Figure 2. The carbon concentrations are marked with red dashed lines in these

isopleths. All compositions have hypereutectic carbon concentrations and as silicon content increases the carbon content decreases in the cast irons (Figure 2), due to its decrease in the eutectic transformation.<sup>[28]</sup> Phase transformations start with nucleation of the graphite ( $G$ ) from the liquid phase ( $L$ ) for all compositions, followed with precipitation of MC carbide and austenite ( $A$ ) crystallization from the liquid. As cooling proceeds, ferrite ( $F$ ) starts to form from the austenite and the transformation is completed at  $A_1$  temperature. All cast irons have ferrite, MC carbide and graphite phases at  $RT$ . Even though, all cast irons have same transformation sequence and same  $RT$  phases, the silicon content affects the transformation temperatures and phase fields. As the silicon content increases in the cast iron, (i) the primary MC carbide becomes stable at higher temperatures resulting in the expansion of L-MC phase field since silicon has not only graphitization potential but also it promotes carbide formation during solidification due to its inverse segregation,<sup>[29]</sup> (ii) ferritic phase field increases causing the decrease of  $A + G + MC$  phase field due to its high solubility in ferrite, as a result of which austenite transformation to ferrite shifts to higher temperatures and as it can be seen at the highest silicon content (7 wt pct),  $A + G + MC$  phase field almost disappears and crystallization of ferrite can be observed followed by eutectic reaction,<sup>[28]</sup> (iii) a significant increase in  $A_1$  is determined as shown in Figure 3. Considering the lowest (4 wt pct) and the highest (7 wt pct) silicon contents the obtained  $A_1$  temperatures are 853 °C and 1065 °C, respectively.

The variation of graphite and MC carbide mole fractions as a function of silicon content for the studied compositions are calculated and given in Figure 4. It is a fact that silicon promotes nucleation of graphite, increasing the number of graphite nodules,<sup>[30,31]</sup> however, as the silicon content increases graphite mole fraction decreases due to the decreasing carbon content in the studied compositions (Figure 4(a)). On the other hand, increasing silicon content causes a decrease in cooling rate during solidification which slows down the carbon diffusion to the graphite nodules that are surrounded by austenite. Therefore, it is expected that the growth of graphite nodules is inhibited.<sup>[32]</sup> Although MC carbide formation during solidification is promoted by increasing silicon content as discussed above, the slight decrease in MC mole fraction shown in Figure 4(b) can be attributed to the decrease in carbon content in the liquid phase.

In order to show the phases present in the microstructures of the cast irons at  $RT$ , SEM micrographs of 4SiNb and 7SiNb cast irons are given in Figure 5. In the microstructure of 4SiNb, graphite nodules embedded in

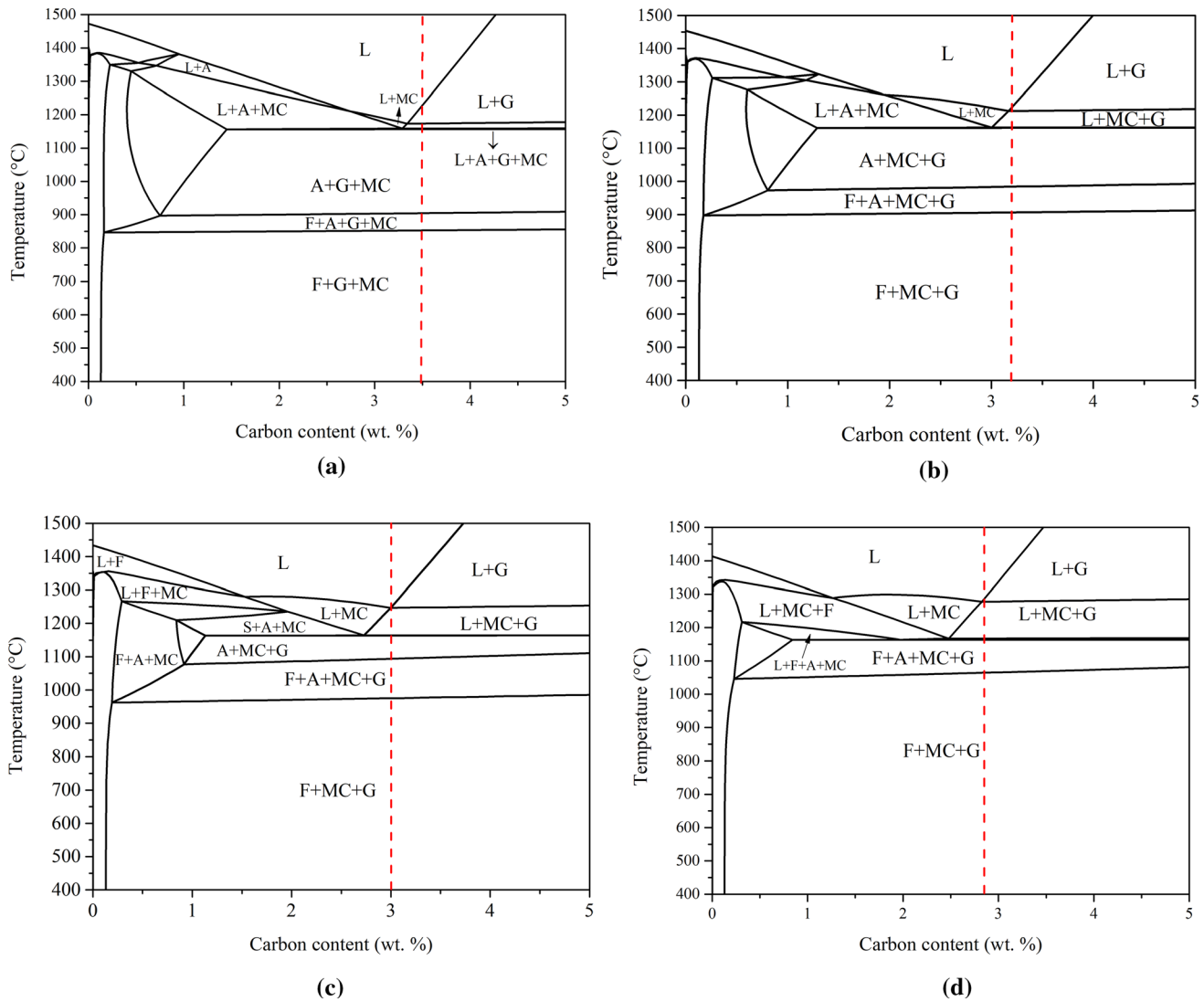


Fig. 2—The C-isopleths of  $x$ SiNb cast irons; (a) 4SiNb, (b) 5SiNb, (c) 6SiNb and (d) 7SiNb.

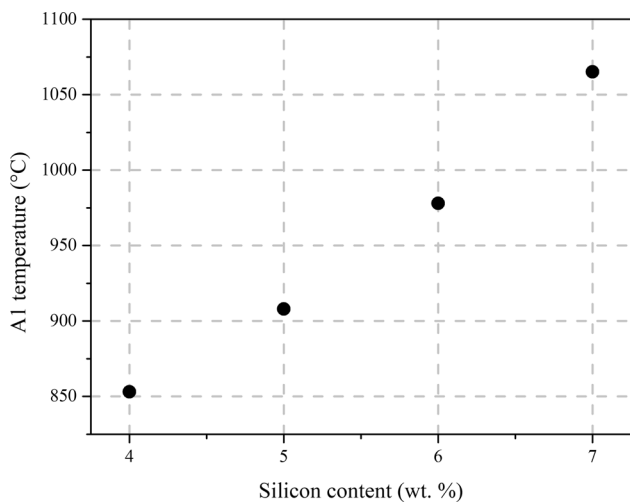


Fig. 3—The effect of silicon content on  $A_1$  temperatures of the studied cast irons.

ferrite, pearlitic (P) regions at cell boundaries with precipitates within them are observed along with faceted precipitates. In order to identify the nature of the precipitates in the microstructure, EDS analyses are carried out at points #1 and #2 shown in Figure 5(a). The results reveal that the faceted carbide at #1 is NbC with a composition of 93.42 wt pct Nb, 6.58 wt pct C. The studies have shown that faceted primary MC type carbides form in ductile cast irons modified by niobium.<sup>[33,34]</sup> The precipitate within the pearlitic region (#2) has a composition of 2.75 wt pct C, 97.25 wt pct Fe indicating the presence of an iron rich  $M_3C$  carbide. As it is known  $M_3C$  type carbide can be present in the ledeburitic structure as a result of eutectic transformation in cast irons.<sup>[35–39]</sup> The presence of pearlitic regions and  $M_3C$  carbides at cell boundaries are caused by elemental microsegregation that takes place during solidification in ductile cast irons.<sup>[40,41]</sup> The negative segregation of silicon and positive segregation of manganese promote the formation of  $M_3C$  type carbide at cell boundaries during solidification along with the

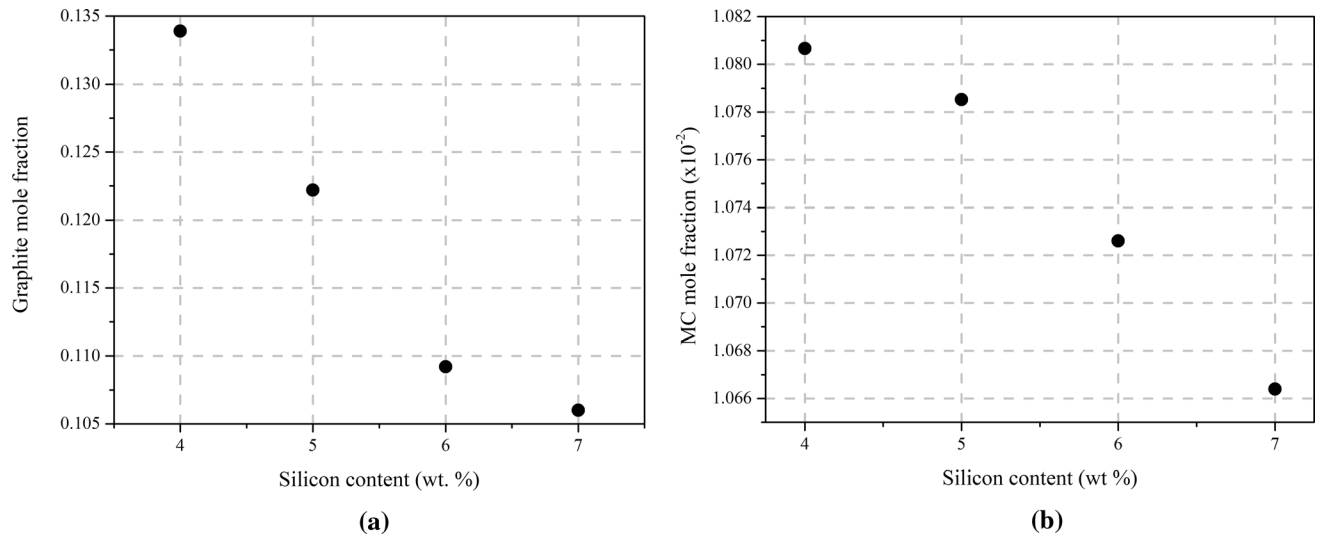


Fig. 4—Calculated (a) graphite and (b) MC mole fractions as a function of silicon content for the studied compositions.

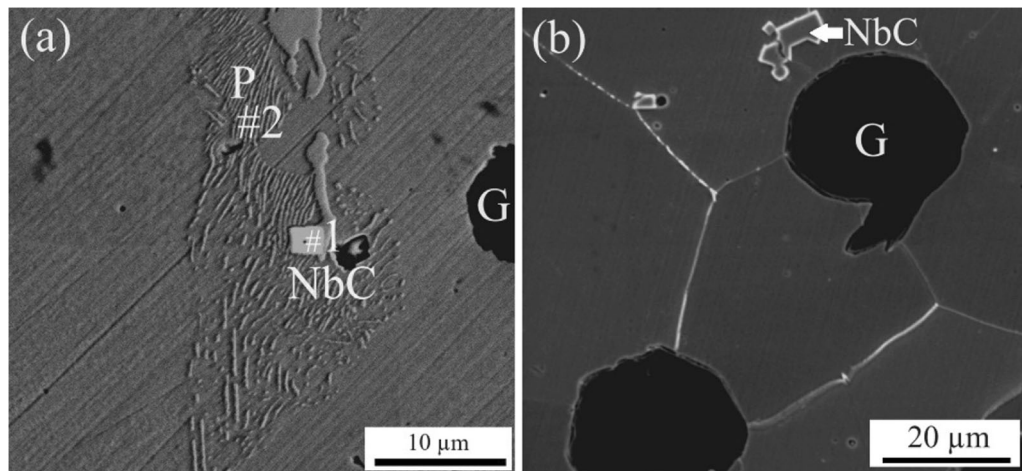


Fig. 5—SEM micrographs of (a) 4SiNb and (b) 7SiNb cast irons.

eutectic transformation and such microsegregations also promote pearlite transformation during eutectoid reaction.<sup>[40,41]</sup> It is known that silicon suppresses cementite precipitation and manganese promotes cementite precipitation by taking place within the cementite<sup>[42]</sup> and as seen in Figure 5(b), a full ferritic matrix having no pearlitic structure is observed in the microstructure of 7SiNb cast iron. The XRD spectra given in Figure 6 also help to identify the microstructural features and are consistent with the SEM observations. The increasing silicon content inhibits cementite precipitation as discussed above; thus, cementite peak does not appear especially in 6SiNb and 7SiNb cast irons' spectra. Even though Thermo-Calc calculations do not indicate the formation of pearlitic structure, due to the local segregation presence of pearlitic regions within the solidified structure is inevitable.

Image analysis is used to calculate the amounts of phases in the cast irons and results are given in Table III. The graphite content decreases as silicon content

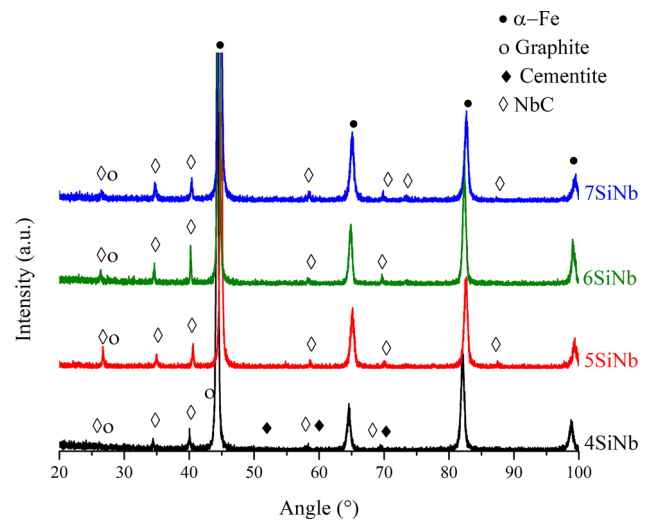


Fig. 6—XRD patterns of the studied cast irons.

increases in the cast irons as calculated by Thermo-Calc. The studies have shown that silicon takes place in graphite crystal and promotes its nucleation causing an increase in the number of graphite,<sup>[30,31]</sup> besides graphite morphology depends on the solidification rate.<sup>[32]</sup> The decrease in cooling rate causes slower encapsulation of graphite by austenite, thus graphite content in the matrix decreases due to the inhibited growth of nucleated graphite, besides nodular morphology of graphite is deteriorated.<sup>[32,43]</sup> This effect of cooling rate becomes clearer as the silicon content gets over an optimum value (max. 5 wt pct). Although all cast irons have the same Nb content, NbC amount in the solidified volume changes and it decreases as the silicon amount increases causing a decrease in carbon content to optimize the carbon equivalent. On the other hand, as the silicon content increases localized pearlitic regions decrease in the microstructures (Figure 7) and disappear completely in the 6SiNb and 7SiNb cast irons. As silicon content reaches to 6 wt pct, despite its inverse segregation, the amount dissolved at cell boundaries is high enough to avoid cementite precipitation.

The solidification of hypereutectic ductile cast irons starts by nucleation of graphite from liquid and growth of graphite during solidification takes place by the diffusion of carbon from liquid. As cooling continues the graphite nodules are encapsulated by austenite that nucleates from liquid, therefore carbon has to pass through austenite for the growth of encapsulated graphite. In case of slow cooling, encapsulation of graphite nodules by austenite happens at a slower rate and carbon diffusion takes place from liquid at a higher rate at unencapsulated regions as a result of which graphite grows towards liquid phase and its nodularity gets deteriorated. At higher cooling rates, the graphite nodule is homogeneously encapsulated by austenite and carbon diffusion continues through austenite all around graphite causing its growth in nodular morphology.<sup>[32,43]</sup> As silicon content in the liquid composition increases the supercooling at the austenite-liquid interface is affected and increased silicon content causes lower cooling rate.<sup>[26,30–32,44]</sup> Chen *et al.* have reported that besides silicon effect, graphite nodularity is also affected by niobium which decreases carbon diffusion.<sup>[34]</sup> Besides the chemical composition of the cast iron,<sup>[14]</sup> quality and efficiency of inoculation and spheroidization treatments during casting also affect the graphite nodularity as well as the composition of the agents used.<sup>[30,31,45]</sup> The graphite morphologies of the studied cast irons are classified according to DIN EN ISO 945-2 and the change in morphology is evaluated with respect to the increasing silicon content. In

Figure 8, the LM images of the polished samples used in image analyses are given. The standard describes the graphite morphologies as; vermicular (III), semi-spheroidal (V), spheroidal (VI) and unclassified (other). The image analyses data for graphite morphology is given in Table IV. In all cast irons, the dominant morphology is semi-spheroidal (V) and as silicon content of the cast iron increases the vermicular graphite (III) increases and nodularity decreases (V and VI). Earlier studies have shown that the decrease in cooling rate due to increased silicon content causes the loss of nodularity of graphite.<sup>[26,30,31,44]</sup>

## B. Solidification Sequence and Microsegregation

The determination of the solidification behavior of the studied cast irons is important for controlling their castability and microstructural features. The Scheil module of Thermo-Calc software provides models to determine the temperatures where the solidification starts and finishes and the temperature range where the cast iron can be cast. It also provides information about the phase transformations during solidification and their temperatures, thus helps to decide on the casting procedures for controlling microstructural features. In case of casting, a cast iron having a primary carbide forming element like niobium in its composition, the size and distribution of carbides can be controlled by the knowledge of temperature range for the carbide formation. The solidification curves calculated for the cast irons are given in Figure 9. In all cast irons, solidification starts from the liquid by the nucleation of graphite. Since the  $C_{eq}$  values of the compositions are close to each other, the critical temperatures for the start of solidification ( $T_L$ ) are similar, but as silicon content increases it changes between 1229 °C and 1279 °C. After graphite transformation (L + G), MC carbide crystallizes from the liquid (L + G + MC) and the solidification is completed by austenite transformation (L + G + MC + A) in 4SiNb, 5SiNb and 6SiNb cast irons. On the other hand, solidification is finalized after austenite transformation by crystallization of ferrite (L + G + MC + A + F) in 7SiNb cast iron. Earlier studies have shown that at higher silicon contents solidification of the cast iron from liquid is completed by ferrite crystallization from liquid.<sup>[26]</sup> However, this takes place at a very narrow temperature range (~ 1 °C) and can be ignored in practical applications. The solidification temperatures ( $T_S$ ) of the studied cast irons increase as their silicon contents increase and vary between 1148 °C and 1163 °C. The solidification ranges ( $T_L-T_S$ ) of the cast irons are suitable for practical casting applications.

The phase transformation temperatures can be determined by thermal analyses<sup>[46,47]</sup> and in order to compare the solidification range of the cast irons with the calculated values, the DTA thermogram is useful in determining both  $T_L$  and  $T_S$  temperatures in the cooling condition. The DTA thermogram is used in the heating condition to determine the  $A_1$  temperature (Figure 10), which can reflect the high temperature properties of cast irons and is an important phase transformation

**Table III. Amount of Phases Determined by Image Analyses (Area Pct)**

Cast Iron	Graphite	NbC	Pearlite
4SiNb	7.3 ± 0.3	1.13 ± 0.04	0.05 ± 0.010
5SiNb	6.9 ± 0.3	1.10 ± 0.03	0.02 ± 0.005
6SiNb	6.4 ± 0.4	1.07 ± 0.05	—
7SiNb	6.1 ± 0.2	1.04 ± 0.04	—

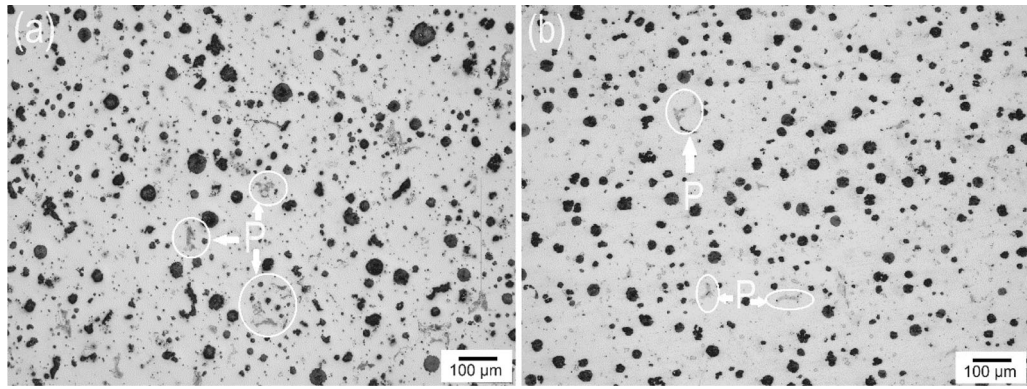


Fig. 7—The LM images showing the pearlitic regions within the cast structures of 4SiNb (a) and 5SiNb (b).

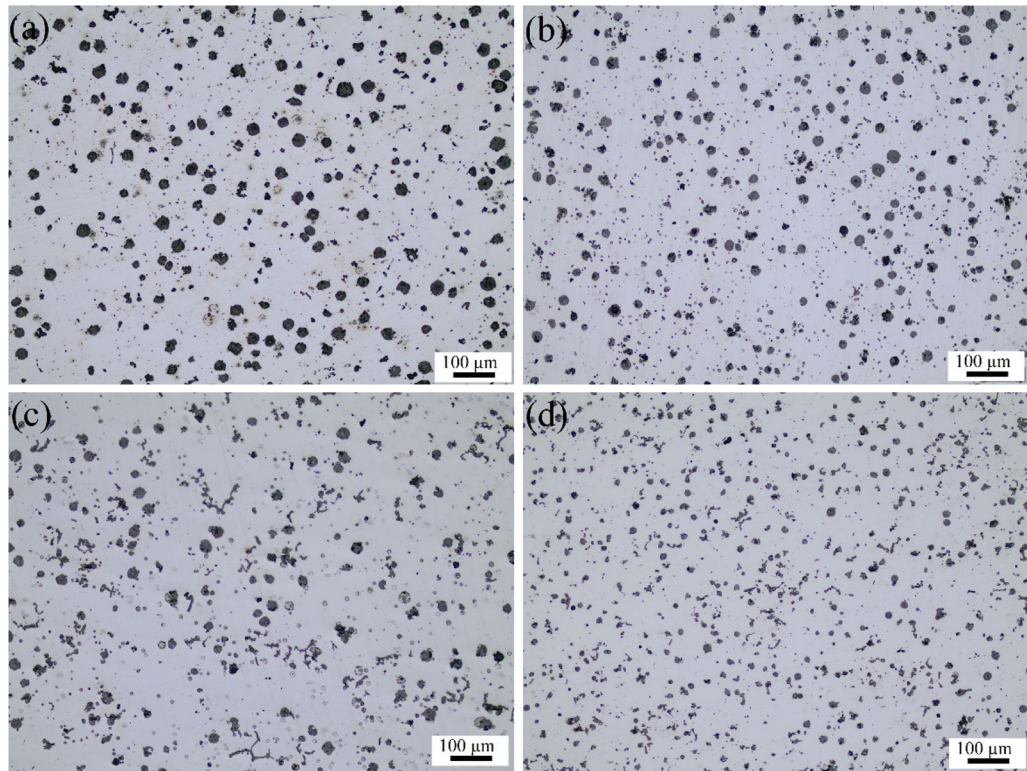


Fig. 8—LM images of the polished samples used in image analyses (a) 4SiNb, (b) 5SiNb (c) 6SiNb and (d) 7SiNb.

temperature. In Table V, the critical temperatures are given as a list and compared with the calculated values. As can be seen from Table V, there are slight differences between the calculated (T-C) and measured (DTA) values which may be related with the presence of Mn, Mg, P, S and other trace elements in the real compositions. On the other hand, it's a fact that the selected heating/cooling rate affects all critical temperatures in DTA measurements. Thus, this discrepancy between calculated and measured values depends on not only chemical variation but also the effect of kinetics. The crystallization temperatures of graphite, MC carbide and austenite from liquid under cooling condition can be followed and they are denoted by  $T_G$ ,  $T_{MC}$  and  $T_A$ , respectively in Figure 10(a). By considering heating

condition given in Figure 10(b), the ferrite transformation temperature ( $T_F$ ) from austenite and eutectoid transformation temperature ( $A_1$ ) are also shown. Thermograms in heating condition have revealed that as silicon content increases both  $T_F$  and  $A_1$  temperatures shift to higher values. In the heating thermogram of 7SiNb cast iron,  $A_1$  reaches to 1000 °C and  $T_F$  peak cannot be identified. By considering the isopleths given in Figure 2, it is clear that as silicon content increases ferrite phase field expands and  $A_1$  temperature shifts to higher temperatures. In this case, as silicon content changes from 4 to 7 wt pct, it is inevitable that a difference of 153 °C appears. It is also clear that the  $A_1$  temperatures are constant in isopleth of each composition even though carbon content varies. In calculation,

Nb content is kept at a constant value as 1 wt pct to avoid its effect on  $A_1$  temperature. In castings both Si and Nb contents vary approximately  $\pm 0.05$  wt pct compared to nominal compositions, which should be considered as negligible. When its isopleth calculated by Thermo-Calc is examined, it can be seen that the  $A + G + MC$  phase area is very small to be identified and the phase area  $F + A + G + MC$  starts just below the eutectic temperature where ferrite transforms from liquid. Thus, it can be concluded that  $T_F$  and  $T_A$  overlap in the thermogram of this cast iron. However, as can be

**Table IV. Change in Graphite Morphology in the Studied Cast Irons (Area Pct)**

Cast Iron	Graphite Morphology (Area Pct)			Other
	III	V	VI	
4SiNb	11.3	54.1	28.8	5.7
5SiNb	12.1	53.6	31.0	3.2
6SiNb	21.1	49.9	21.9	7.1
7SiNb	20.8	49.3	23.4	6.5

seen from Figure 10(a), when the cooling thermogram of 7SiNb cast iron is considered,  $T_F$  is determined as 1150 °C, and when this temperature is reached, ferrite crystallizes from the liquid. González-Martínez *et al.* have shown that in a cast iron having 9 wt pct Si, no peak can be determined for eutectoid transformation in thermal analyses studies and the solidification of the cast iron is completed by ferrite crystallization and no other transformation occurs during cooling down to RT.<sup>[26]</sup>

The mole fraction of the phases during solidification are calculated by Thermo-Calc and phase profiles are determined as given in Figure 11. The “0” point indicates liquid phase and “1” point indicates completion of solidification. The graphite profiles during solidification of the cast irons are given in Figure 11(a). In all the cast irons, graphite nucleation starts at the beginning of the solidification and rapid increase is observed in its content. Graphite formation continues till the end of solidification, and it changes linearly. Slope change can be seen in 7SiNb cast iron profile at 0.3 mole fraction of solid, indicating the formation of another phase (ferrite as it will be discussed below). Due to the similar  $C_{eq}$  values of the cast irons, only small changes are observed in the amount of graphite formed at the end of the solidification. The MC carbide nucleation starts at the beginning of the solidification similar to the case of graphite (Figure 11(b)). MC amount at the end of solidification is similar for all

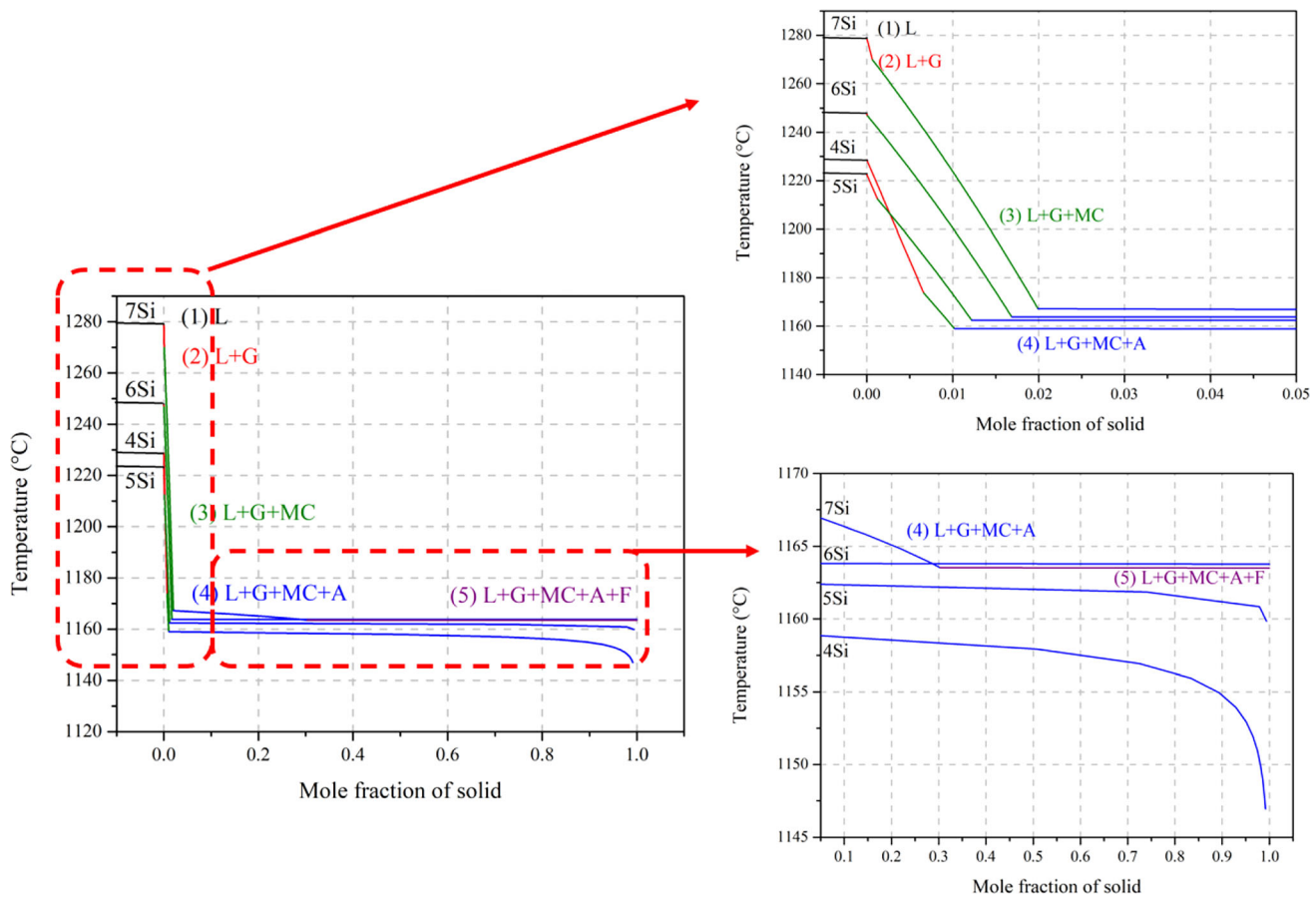


Fig. 9—Solidification sequence of  $x$ SiNb cast irons.



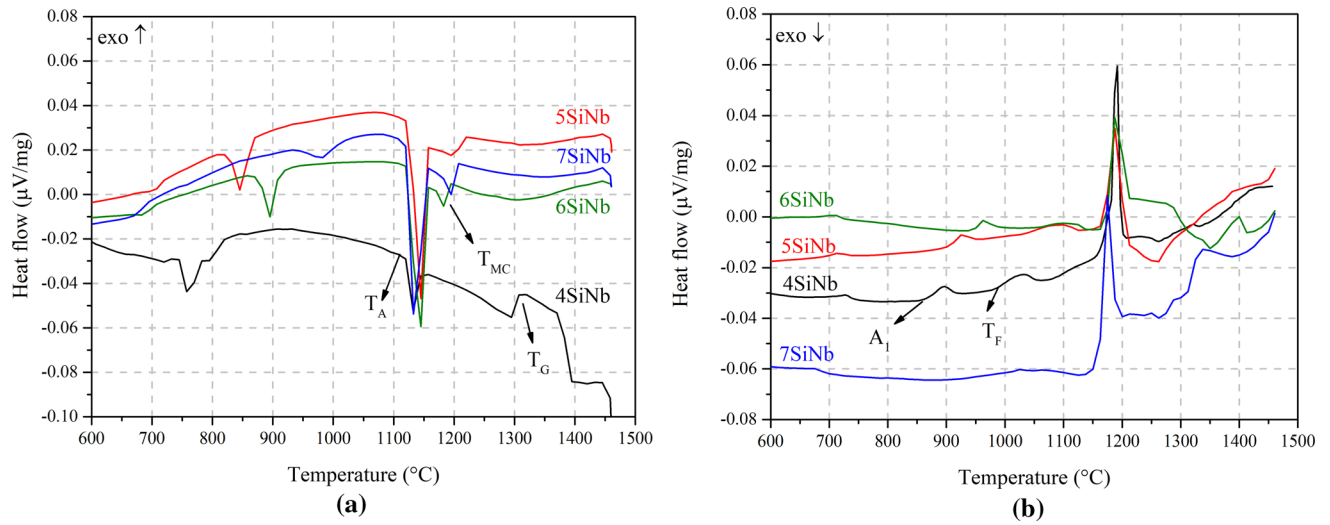


Fig. 10—DTA thermograms of the studied cast irons for (a) cooling and (b) heating.

**Table V. Critical Temperatures of Cast Irons Identified by Calculations (T-C) and DTA (°C)**

Cast Iron	$T_G$		$T_{MC}$		$T_A$		$T_F$		$A_1$	
	T-C	DTA	T-C	DTA	T-C	DTA	T-C	DTA	T-C	DTA
4SiNb	1229	1289	1174	1244	1160	1160	902	976	853	860
5SiNb	1223	1312	1212	1270	1162	1158	972	1054	916	912
6SiNb	1248	1305	1246	1278	1164	1162	1102	1112	975	951
7SiNb	1279	1321	1270	1268	1164	1150	1148	1150	1065	1013

cast irons, it is only slightly affected by their silicon content. According to the literature, elements that promote graphite formation in cast irons cause a decrease in carbide formation due to the decreased carbon content in the liquid phase.<sup>[29,48]</sup> In all the studied cast irons, crystallization of the austenite phase from liquid starts right after the formation of graphite and MC carbide and continues till the end of the solidification (Figure 11(c)). In the profile of 7SiNb cast iron given in Figure 11(d), a slope change is observed at 0.3 mole fraction of solid which clearly indicates formation of ferrite phase resulting in a decrease in austenite content.

Calculations indicate that the first phase to crystallize from the liquid is the austenite phase. Thus, elemental segregation in solidification is followed by the partition of solute element atoms at the liquid–austenite interface. The partition coefficient ( $k$ ) gives the ratio of the elemental concentration in the solid phase to the elemental concentration in the liquid phase. If  $k$  is less than 1 during solidification, the liquid phase is enriched in elements. In the process where the solidifying phase from the liquid is austenite, microsegregation is characterized by partition coefficient ( $k_\gamma$ ) of the austenite phase. In the austenite phase, the amount of segregation of elements (C, Nb) with a low partition coefficient (in the case of  $k < 1$ ) towards the liquid is higher. As a

matter of fact, in a study in which equilibrium partition coefficient values are calculated with Thermo-Calc software with the CALPHAD approach,<sup>[49]</sup> the  $k_\gamma$  values for carbon and niobium in austenite are calculated as 0.19 and 0.4, respectively. In this case, a positive segregation tendency of these two elements occurs. Silicon is another solute element in the austenite phase, and its relatively higher  $k_\gamma$  value (0.77) compared to these two elements (C and Nb) indicates that it has a negative segregation tendency. In this study, elemental microsegregations within the austenite phase are also calculated during solidification. The elemental profiles showing the changes in the amounts of C, Si, Nb and Mn are given in Figure 12 as a function of the mole fraction of solid. The carbon segregation within austenite is shown in Figure 12(a) and a decrease is observed at the beginning of the solidification due to the nucleation of the graphite. As solidification progresses positive segregation of carbon is observed in all cast irons; however, the segregation is not very strong, the composition of carbon changes only slightly, except towards the end of solidification the amount of carbon in austenite phase increases. These findings are in good agreement with earlier studies reporting positive segregation of carbon in austenite.<sup>[50]</sup> The carbon content in austenite phase decreases in the cast irons as their silicon content increases due to (i) the decrease in the solubility

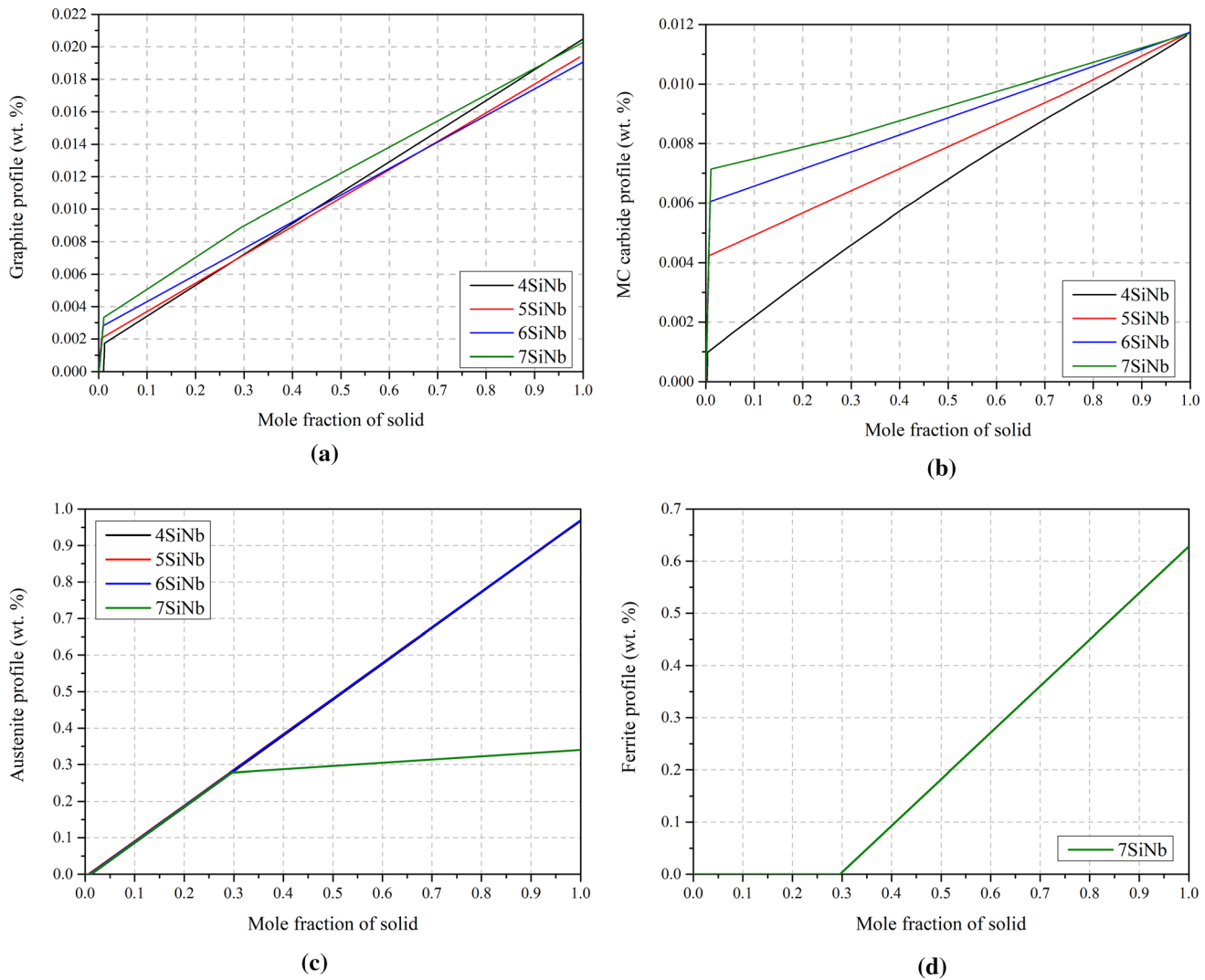


Fig. 11—Phase profiles of the cast irons during solidification; (a) graphite, (b) MC carbide, (c) austenite and (d) ferrite.

of carbon in austenite with the increased silicon content<sup>[51]</sup> and (ii) the decrease in carbon in the chemical composition. The decrease in carbon profile of 7SiNb has a slope change at the mole fraction which ferrite forms and an increase in carbon, dissolved in austenite phase, is observed. Thus, the decrease in carbon mole fraction slows down. The reason why the carbon increases in austenite is due to the increase of carbon in liquid phase since it has low solubility in ferrite.<sup>[50]</sup> The silicon segregation in austenite phase during solidification of the cast irons is given in Figure 12(b). As it is known, silicon has inverse segregation during solidification due to its high solubility in fcc crystal and the silicon mole fraction decreases at austenite cell boundaries.<sup>[40,41,52]</sup> This inverse segregation is observed in all the studied cast irons. In 7SiNb cast iron, the increasing silicon mole fraction in austenite phase slows down due to the formation of ferrite. The silicon solubility in ferrite phase is high and this causes a decrease in silicon content in liquid phase during crystallization of ferrite and causing a decrease in silicon in the austenite phase. The niobium segregation in austenite is given in

Figure 12(c), indicating the decrease in niobium content in the liquid phase at the beginning of solidification when MC carbide starts to precipitate. Thus, a sharp decrease in niobium mole fraction is seen in all cast irons and continuous decrease is observed during solidification. The niobium solubility in austenite decreases as silicon content increases, which has been reported also by Mohrbacher earlier.<sup>[51]</sup> Figure 12(d) shows the positive segregation of manganese in austenite as reported in an earlier study,<sup>[50]</sup> as a result of which manganese mole fraction in austenite continuously increases during solidification.

SEM/EDS studies are carried out at the areas between the graphite nodules and the cell boundaries in order to observe the tendency of elemental microsegregations of C, Si, Nb and Mn and to compare with the results of thermodynamical modelling. The cell boundaries are defined from graphite phase towards pearlite in the matrices of both 4SiNb and 5SiNb cast irons and from graphite phase towards carbide phase in the matrices of both 6SiNb and 7SiNb cast irons which do not have pearlite in their microstructures. The boundaries and the

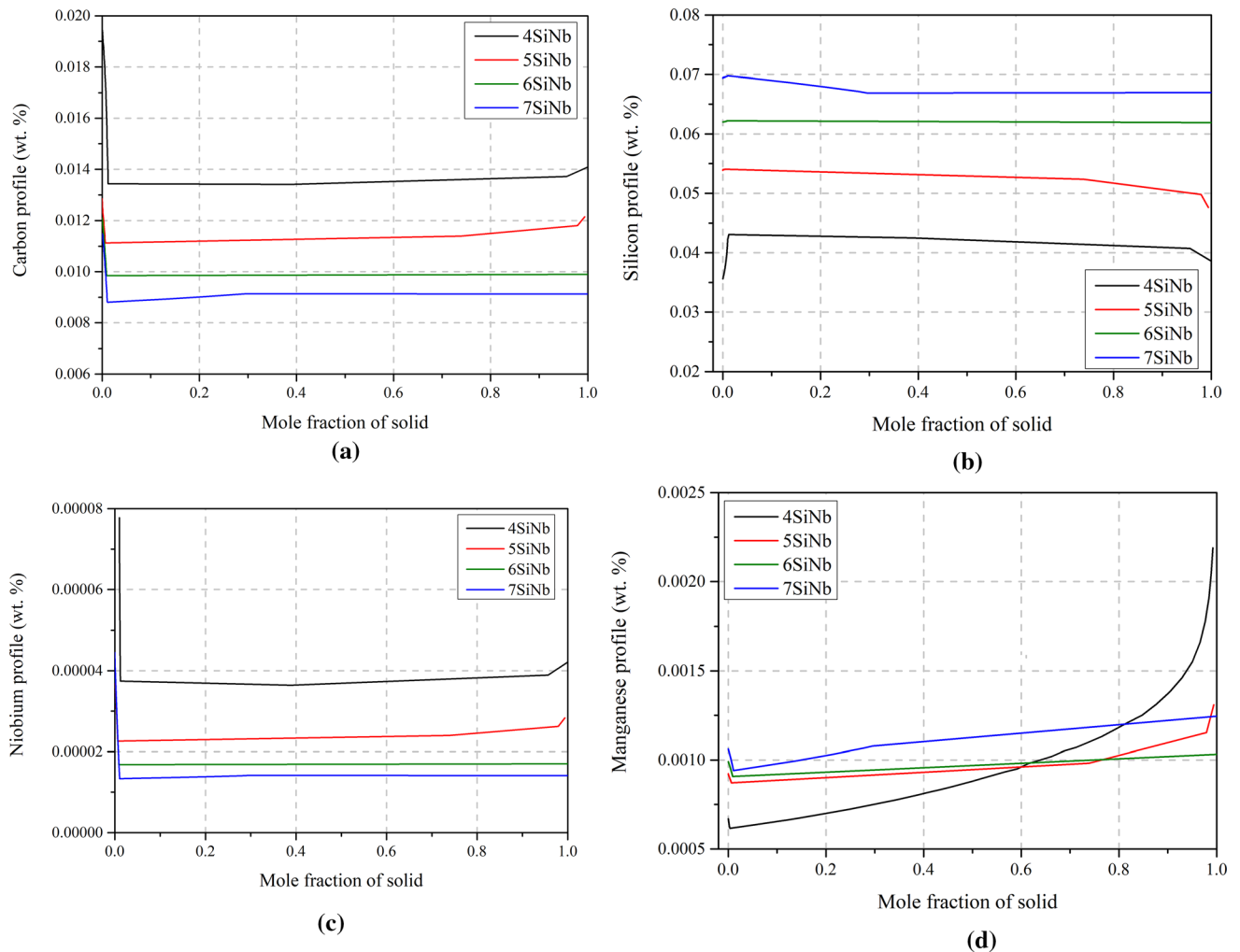


Fig. 12—Element profiles of the austenite phase during solidification; (a) C, (b) Si, (c) Nb and (d) Mn.

points for elemental analyses for 4SiNb and 7SiNb are shown in Figures 13(a) and (b), respectively. The obtained data are used in the scatter plots given in Figure 14 and as can be seen clearly the segregation behavior of the elements are in good agreement with those determined by thermodynamical calculations. As can be seen, the elemental segregation trend determined by EDS analyzes within the defined limits shows a similar trend with the calculated segregation profiles. However, the collection of signals with a certain width and depth at the high acceleration voltage studied, causes the quantitative values to be relatively higher than the calculated ones. During solidification, positive segregation of carbon towards cell boundaries and formation of carbon-rich phases at the boundaries is inevitable (Figure 14(a)). The negative segregation tendency of silicon (Figure 14(b)), as discussed before, leads to the formation of pearlite at the boundaries, however as the silicon content dissolved in the matrices of 6SiNb and 7SiNb cast irons increases pearlite formation is avoided (Table III). The EDS data reveal that niobium, which has solubility in ferrite, shows positive segregation tendency towards cell boundaries

and supports carbide formation at those boundaries in the final solidified structure (Figure 14(c)). Manganese is another pearlite forming element and shows segregation towards the boundaries during solidification (Figure 14(d)). However, due to the dominant effect of silicon, pearlite formation by manganese is limited (Table III).

## V. CONCLUSION

In this study, the solidification behaviors of  $x$ SiNb cast irons, that are designed as alternatives to SiMo cast irons, were CALPHAD-based modeled and cast structures were metallurgically characterized. Modeling studies indicated that the amount of graphite and MC in the ferrite matrix decreased in the final solidification structure due to the increase in silicon content. Quantitative analyses of casting structures had confirmed such a trend. Both modeling and experimental studies indicated that (i) silicon had a negative segregation tendency and such an effect was responsible for the suppression of the formation of pearlite phase at the cell boundaries, (ii)

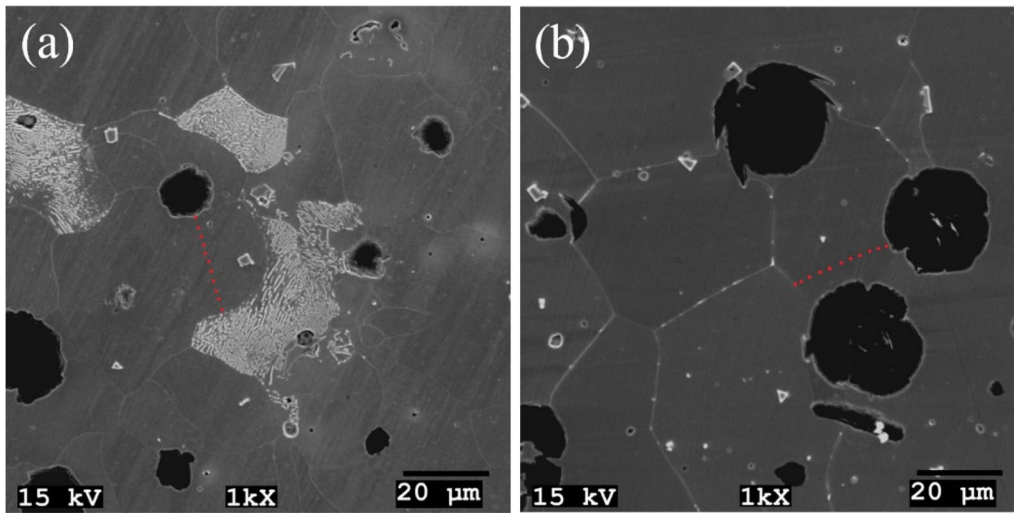


Fig. 13—SEM micrographs used for microsegregation; (a) 4SiNb and (b) 7SiNb.

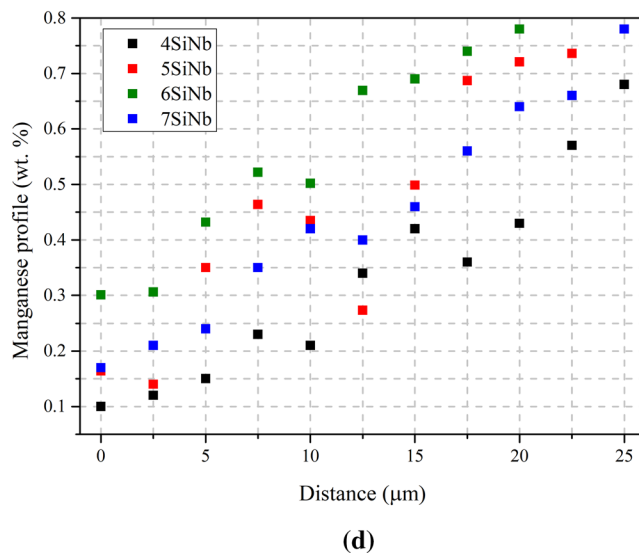
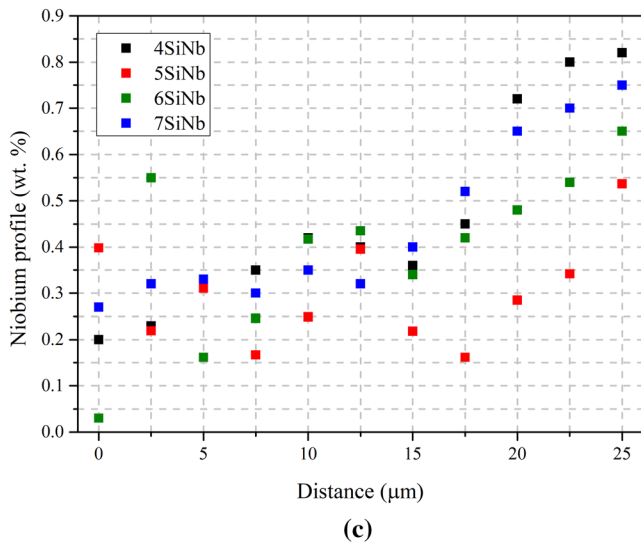
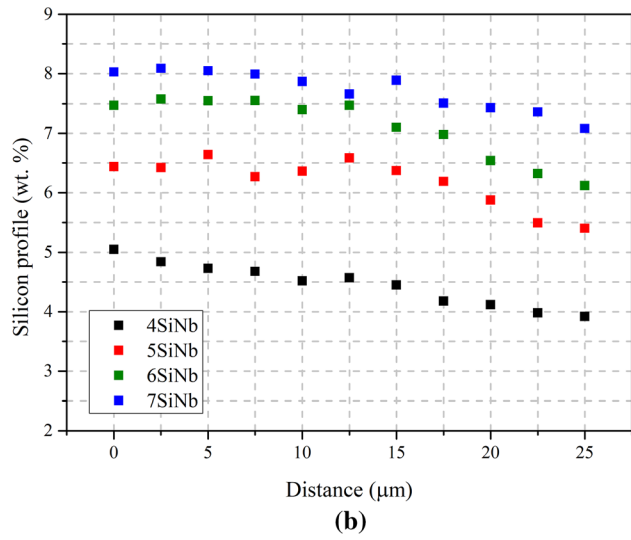
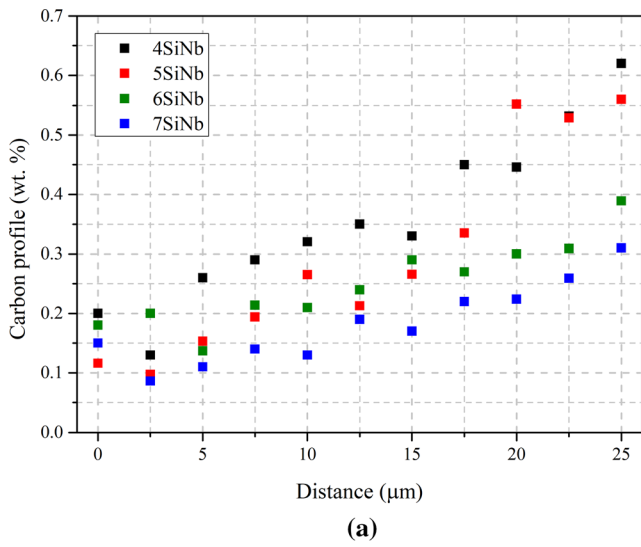


Fig. 14—EDS data showing the elemental segregations in ferrite phase for the studied cast irons; (a) C, (b) Si, (c) Nb and (d) Mn.

silicon content had an increasing effect on  $A_1$  temperature providing the utilization at higher temperatures, and (iii) the highest  $A_1$  temperature as 1013 °C could be obtained at the highest silicon content (7 wt pct).

## ACKNOWLEDGMENTS

The authors wish to acknowledge the financial support given by Scientific Research Projects Coordination Unit of Kocaeli University under the Project Numbers 2017/118 and 2019/118.

## FUNDING

Open access funding provided by the Scientific and Technological Research Council of Türkiye (TÜBİTAK). Open access funding provided by the Scientific and Technological Research Council of Türkiye.

## OPEN ACCESS

This article is licensed under a Creative Commons Attribution 4.0 International License, which permits use, sharing, adaptation, distribution and reproduction in any medium or format, as long as you give appropriate credit to the original author(s) and the source, provide a link to the Creative Commons licence, and indicate if changes were made. The images or other third party material in this article are included in the article's Creative Commons licence, unless indicated otherwise in a credit line to the material. If material is not included in the article's Creative Commons licence and your intended use is not permitted by statutory regulation or exceeds the permitted use, you will need to obtain permission directly from the copyright holder. To view a copy of this licence, visit <http://creativecommons.org/licenses/by/4.0/>.

## COMPETING INTERESTS

The authors declare that they have no known competing financial interests or personal relationships that could have appeared to influence the work reported in this paper.

## REFERENCES

1. C. Xia, T. Zhao, J. Fang, L. Zhu, and Z. Huang: *Front. Energy*, 2022, vol. 16, pp. 900–15. <https://doi.org/10.1007/s11708-021-0812-6>.
2. N. Kumar, B.B. Arora, and S. Maji: *Renew. Energy Optim. Plann Control.*, 2022, [https://doi.org/10.1007/978-981-16-4663-8\\_2](https://doi.org/10.1007/978-981-16-4663-8_2).
3. Y. Zhang, M. Li, L.A. Godlewski, J.W. Zindel, and Q. Feng: *Metall. Mater. Trans. A*, 2016, vol. 47A, p. 3289. <https://doi.org/10.1007/s11661-016-3544-1>.
4. T. Zhao, J. Zhang, and L. Teng: *Trans. Indian Inst. Met.*, 2021, vol. 74, pp. 301–12. <https://doi.org/10.1007/s12666-020-02139-9>.
5. Y. Li, J. Liu, W. Huang, and Y. Wu: *Int. Metalcast.*, 2023, vol. 17, pp. 538–50. <https://doi.org/10.1007/s40962-022-00796-8>.
6. W. Dunlap and A. Druschitz: *SAE Int. J. Mater. Manuf.*, 2010, vol. 3(1), pp. 413–24. <https://doi.org/10.4271/2010-01-0657>.
7. M. Ekström and S. Jonsson: *Mater. Sci. Eng. A*, 2014, vol. 616, pp. 78–87. <https://doi.org/10.1016/j.msea.2014.08.014>.
8. H. Kazdalzeytin, C. Kubilay, H. Aydin, A.A. Ebrinc, and B. Aydemir: *J. Iron Steel Res. Int.*, 2009, vol. 6(3), pp. 32–36. [http://doi.org/10.1016/S1006-706X\(09\)60040-6](http://doi.org/10.1016/S1006-706X(09)60040-6).
9. M.P. Brady, G. Muralidharan, D.N. Leonard, J.A. Haynes, R.G. Weldon, and R.D. England: *Oxid. Met.*, 2014, vol. 82, pp. 359–81. <https://doi.org/10.1007/s11085-014-9496-1>.
10. Y.H. Zhang, M. Li, L.A. Godlewski, J.W. Zindel, and Q. Feng: *Mater. Sci. Eng. A*, 2017, vol. 683, pp. 195–206. <https://doi.org/10.1016/j.msea.2016.12.023>.
11. F. Tholence and M. Norell: *Oxid. Met.*, 2008, vol. 69, pp. 37–62. <https://doi.org/10.1007/s11085-007-9082-x>.
12. Y.L. Yang, Z.Y. Cao, Z.S. Lian, and H.X. Yu: *Adv. Mater. Res.*, 2011, vol. 194–196, pp. 95–99.
13. S.N. Lekakh, A. Bofah, W.-T. Chen, L. Godlewski, and M. Li: *Metall. Mater. Trans. B*, 2020, vol. 51B, pp. 2542–54. <https://doi.org/10.1007/s11663-020-01975-w>.
14. M.M. Ibrahim, M.M. Mourad, A.A. Nofal, and A.I.Z. Farahat: *Int. J. Cast. Met. Res.*, 2017, vol. 30, pp. 61–69. <https://doi.org/10.1080/13640461.2016.1239895>.
15. S. Chandra-ambhorn, T. Tummaporn, and P. Jiradech: *Adv. Mater. Res.*, 2013, vol. 813, pp. 132–35. <https://doi.org/10.4028/www.scientific.net/amr.813.132>.
16. S. Xiang, B. Zhu, and S. Jonsson: *Mater. Sci. Forum*, 2018, vol. 925, pp. 369–76. <https://doi.org/10.4028/www.scientific.net/MSF.925.369>.
17. C. Delprete and R. Sesana: *Mater. Des.*, 2014, vol. 57, pp. 528–37. <https://doi.org/10.1016/j.matdes.2014.01.002>.
18. M. Ekström, P. Szakalos, and S. Jonsson: *Oxid. Met.*, 2013, vol. 80, pp. 455–66. <https://doi.org/10.1007/s11085-013-9389-8>.
19. M. Stawarz: *Arch. Foundry Eng.*, 2017, vol. 17, pp. 147–52. <https://doi.org/10.1515/afe-2017-0027>.
20. M. Stawarz and P.M. Nuckowski: *Materials*, 2020, vol. 13, p. 1745. <https://doi.org/10.3390/ma13071745>.
21. G. Aktaş Çelik, Ş.H. Atapek, Ş. Polat, M.-I.T. Tzini, and G.N. Haide-menopoulos: *Metall. Mater. Trans. A*, 2022, vol. 53A, pp. 1991–2003. <https://doi.org/10.1007/s11661-022-06632-2>.
22. A. Ebel, O. Marsan, J. Lacaze, and B. Malard: *Corros. Sci.*, 2021, vol. 192, 109854. <https://doi.org/10.1016/j.corsci.2021.109854>.
23. G. Aktaş Çelik, M. I. T. Tzini, Ş. H. Atapek, Ş. Polat, and G. N. Haide-menopoulos: 19. International Metallurgy and Materials Congress, Proceedings, 25–27 October 2018, pp. 1086–1089, Istanbul-Turkey.
24. S.H. Park, J.M. Kim, H.J. Kim, S.J. Ko, H.S. Park, and J.D. Lim: *SAE Tech. Paper*, 2005, <https://doi.org/10.4271/2005-01-1688>.
25. G.A. Çelik, M.I.T. Tzini, Ş. Polat, Ş.H. Atapek, and G.N. Haide-menopoulos: *Int. J. Miner. Metall. Mater.*, 2020, vol. 27, pp. 190–99. <https://doi.org/10.1007/s12613-019-1876-8>.
26. R. González-Martinez, U. Torre, A. Ebel, J. Lacaze, and J. Sertucha: *Mater. Sci. Eng. A*, 2018, vol. 712, pp. 794–802. <https://doi.org/10.1016/j.msea.2017.11.050>.
27. R. González-Martinez, U. Torre, A. Ebel, J. Lacaze, and J. Sertucha: *Mater. Sci. Eng. A*, 2018, vol. 712, pp. 803–11. <https://doi.org/10.1016/j.msea.2017.11.051>.
28. ASM Handbook: *Properties and Selection: Irons, Steels, and High Performance Alloys*, 4th ed. ASM International, Ohio, 1995, pp. 17–210.
29. M. Riebisch, B. Pustal, and A. Bührig-Polaczek: *Inter. Metalcast.*, 2020, vol. 14, pp. 1152–61. <https://doi.org/10.1007/s40962-020-00442-1>.
30. U. Torre, J. Lacaze, and J. Sertucha: *Int. J. Mater. Res.*, 2016, vol. 107(11), pp. 1041–50. <https://doi.org/10.3139/146.111434>.
31. W. Baer: *Int. J. Metalcast.*, 2019, vol. 14, pp. 454–88. <https://doi.org/10.1007/s40962-019-00363-8>.
32. B. Bauer, I.M. Pokopec, M. Petric, and P. Mrvar: *Mater. Sci. Forum*, 2018, vol. 925, pp. 70–77. <https://doi.org/10.4028/www.scientific.net/MSF.925.70>.

33. T.N.F. Souza, R.A.P.S. Nogueira, F.J.S. Franco, M.T.P. Aguilar, and P.R. Cetlin: *Mater. Res.*, 2014, vol. 17(5), pp. 1167–72. <https://doi.org/10.1590/1516-1439.249413>.
34. X. Chen, J. Xu, H. Hu, H. Mohrbacher, M. Kang, W. Zhang, A. Guo, and Q. Zhai: *Mater. Sci. Eng. A.*, 2017, vol. 688, pp. 416–28. <https://doi.org/10.1016/j.msea.2017.01.032>.
35. G. Laird II., R.L. Nielsen, and N.H. Macmillan: *Metall. Trans. A*, 1991, vol. 22A, pp. 1709–19. <https://doi.org/10.1007/BF02646494>.
36. V. Randle and G. Laird II.: *J. Mater. Sci.*, 1993, vol. 28, pp. 4245–49. <https://doi.org/10.1007/BF00351261>.
37. C.G. Schön and A. Sinatora: *Calphad*, 1998, vol. 22(4), pp. 437–48. [https://doi.org/10.1016/S0364-5916\(99\)00003-6](https://doi.org/10.1016/S0364-5916(99)00003-6).
38. A. Bedolla-Jacuinde, M.W. Rainforth, and I. Mejia: *Metall. Mater. Trans. A*, 2013, vol. 44A, pp. 856–72. <https://doi.org/10.1007/s11661-012-1434-8>.
39. J. Feng, C. Pan, L. Lu, Q. Huang, and H. Cao: *J. Iron Steel Res. Int.*, 2016, vol. 23(6), pp. 618–24. [https://doi.org/10.1016/S1006-706X\(16\)30096-6](https://doi.org/10.1016/S1006-706X(16)30096-6).
40. A. Alhussein, B. Risbet, A. Bastien, J.P. Chobaut, D. Balloy, and J. Favergeon: *Mater. Sci. Eng. A*, 2014, vol. 605, pp. 222–28. <https://doi.org/10.1016/j.msea.2014.03.057>.
41. J. Lacaze: *Acta Mater.*, 1999, vol. 47(14), pp. 3779–92. [https://doi.org/10.1016/S1359-6454\(99\)00233-5](https://doi.org/10.1016/S1359-6454(99)00233-5).
42. D. Delagnes, P. Lamesla, M.H. Mathon, N. Mebarki, and C. Levallant: *Mater. Sci. Eng. A*, 2005, vol. 394, pp. 435–44. <https://doi.org/10.1016/j.msea.2004.11.050>.
43. J. Zhou, W. Schmitz, and S. Engler: *Giessereiforschung*, 1987, vol. 39, pp. 55–70.
44. J. Sertucha, R. Suárez, I. Asenjo, P. Larrañaga, J. Lacaze, I. Ferrer, and S. Armendariz: *ISIJ Int.*, 2009, vol. 49(2), pp. 220–28. <https://doi.org/10.2355/isijinternational.49.220>.
45. D. Li: *Metall. Mater. Trans. B*, 2018, vol. 49B, pp. 858–59. <https://doi.org/10.1007/s11663-018-1184-0>.
46. D.M. Stefanescu: *Science and Engineering of Casting Solidification*, 2nd ed. Springer, New York, 2009.
47. J. Lacaze, I. Asenjo, S. Méndez, J. Sertucha, P. Larrañaga, and R. Suárez: *Int. J. Metalcast.*, 2012, vol. 6, pp. 35–42. <https://doi.org/10.1007/BF03355476>.
48. A. Shayesteh-Zeraati, H. Naser-Zoshki, A.R. Kiani-Rashid, and M.R. Yousef-Sani: *Mater. Des. Appl.*, 2010, vol. 224(3), pp. 117–22. <https://doi.org/10.1243/14644207JMDA302>.
49. D. Zhang: Characterisation and modelling of segregation in continuously cast steel slab, Thesis of Doctor of Philosophy, September 2015, School of Metallurgy and Materials, College of Engineering and Physical Sciences The University of Birmingham. <http://etheses.bham.ac.uk/id/eprint/6256>.
50. J. Eiken, and J. Lacaze: *Proceedings of the 6th decennial international conference on solidification processing*, Old Winsor, UK, 25–28 July 2017.
51. H. Mohrbacher: On the metallurgical effects of niobium in cast Irons, *WFO*, 2018.
52. S.N. Lekakh, V.L. Richards, and N. Medvedeva: *AFS Proc.*, 2012, vol. 12–031, pp. 1–9.

**Publisher's Note** Springer Nature remains neutral with regard to jurisdictional claims in published maps and institutional affiliations.